



## UvA-DARE (Digital Academic Repository)

### Glow with the flow: Quantifying blood flow and photoluminescence signal in biological tissue

Nadort, A.

**Publication date**

2015

**Document Version**

Final published version

[Link to publication](#)

**Citation for published version (APA):**

Nadort, A. (2015). *Glow with the flow: Quantifying blood flow and photoluminescence signal in biological tissue*. [Thesis, fully internal, Universiteit van Amsterdam].

**General rights**

It is not permitted to download or to forward/distribute the text or part of it without the consent of the author(s) and/or copyright holder(s), other than for strictly personal, individual use, unless the work is under an open content license (like Creative Commons).

**Disclaimer/Complaints regulations**

If you believe that digital publication of certain material infringes any of your rights or (privacy) interests, please let the Library know, stating your reasons. In case of a legitimate complaint, the Library will make the material inaccessible and/or remove it from the website. Please Ask the Library: <https://uba.uva.nl/en/contact>, or a letter to: Library of the University of Amsterdam, Secretariat, P.O. Box 19185, 1000 GD Amsterdam, The Netherlands. You will be contacted as soon as possible.



# 8

---

## DISCUSSION AND CONCLUSION

---

Parts in this chapter are from the following co-authored publications:

Ref. 63

K. Liu, J. A. Holz, Y. Ding, X. Liu, Y. Zhang, T. Langping, X. Kong, B. Priem, **A. Nadort**, S. A. G. Lambrechts, M. C. G. Aalders, W. J. Buma, P. D. Y. Liu, and H. Zhang, "Targeted labeling of early-stage tumor spheroid in chorioallantoic membrane model with upconversion nanoparticles," *Nanoscale* (2014).

Ref. 66

A. E. Guller, A. N. Generalova, E.V. Petersen, A.V. Nechaev, I.A. Trusova, N.N. Landyshev, **A. Nadort**, E.A. Grebenik, S.M. Deyev, A.B. Shekhter and A.V. Zvyagin, "Cytotoxicity and non-specific cellular uptake of bare and surface-modified upconversion nanoparticles in human skin cells," *Nano Research* (2014).

8

**ABSTRACT** This Chapter reflects on the two main research lines of this thesis that focus on optical techniques to assess biological tissues based on (1) laser speckle flowmetry and (2) photoluminescent signals from upconversion nanoparticles. The results presented in this thesis are summarized and their contributions to clinically relevant applications are discussed. Additional results obtained during this PhD project are included, as well as possibilities for further improvements of the techniques.

## 8.1 INTRODUCTION

Optical techniques to assess microcirculation functionality are indispensable for the diagnosis, monitoring, therapy guidance and understanding of many diseases ranging from the onset of septic shock to the delivery of drugs to tumours. This thesis contributes to the development of optical techniques to improve the assessment of microcirculation pathology and drug delivery in a minimally invasive way. The first part of this thesis aims to develop a non-invasive and quantitative technique to assess the microcirculatory blood flow based on laser speckle flowmetry. The second part is devoted to the quantification of optical signals arising from photoluminescent upconversion nanoparticles (UCNPs) in the context of sensitive detection in biomedical tissues, in particular vascularised tumour tissue. In this discussion chapter, I will review the two main research lines individually, including the contribution to clinically relevant applications of the results presented in this thesis, additional results and future improvements. In the final Chapter 9, I will present a general conclusion and outlook on how the techniques can be brought together to serve in the context of cancer diagnosis and treatment monitoring and contribute to the clinical understanding of tumour development.

## 8.2 LASER SPECKLE FLOWMETRY: A QUANTITATIVE TOOL?

### 8.2.1 Key results on laser speckle flowmetry

Chapters 2 through 4 address several theoretical aspects underlying laser speckle flowmetry which chronologically contribute to an increasing accuracy in determining blood flow velocity from speckle decorrelation times, accompanied by experimental validation. Chapter 2 starts with the basic expression on speckle statistics given by Goodman [1] and subsequent derivation presented by Fercher and Briers [2], relating the time-varying speckle fluctuations to the imaged speckle contrast (Eq. 2.8). An important input requirement for correct interpretation is a model describing the temporal autocorrelation function (ACF) of the speckle fluctuations, referred to as  $g_1(\tau)$  which is parameterized by the characteristic decorrelation time  $\tau_c$ . Usually a Lorentzian or Gaussian form of  $g_1(\tau)$  is assumed [3-5], resulting in the speckle contrast Eq. 3.6 (Lorentzian) or 3.7/4.10 (Gaussian) through which  $\tau_c$  can be found from speckle contrast  $K$  (provided that  $\beta_m$  and  $\rho$  are well estimated, for example using a multi-exposure acquisition and subsequent nonlinear curve fit) [6, 7].

The first gap in the speckle literature addressed in this thesis is the relationship between  $\tau_c$  and blood flow velocity  $V$  in tissues *in vivo*. The relationship is often verified to be of the form  $1/\tau_c \sim V$  using flow phantom set-ups [7-9], but a lack of knowledge of actual blood flow velocity limited the verification *in vivo*. The integration of sidestream dark field (SDF) microscopy and laser speckle contrast imaging (LSCI) opened up the possibility to compare both (Chapter 3). Flow phantom experiments confirmed that the SDF-LSCI geometry adequately produces and detects speckle patterns, and that the linear relationship of  $1/\tau_c$  with  $V$  is reproduced.  $K$  was reliably estimated by sufficient sampling of speckles in a spatiotemporal local region of the image pixels, while maintaining a useful spatial and temporal resolution *in vivo*. We found a considerable speckle decorrelation for tissue regions without flow when analyzing *in vivo* speckle contrast images and corresponding SDF images of the microcirculation, with a high correlation between tissue decorrelation times

and adjacent vessel decorrelation times. Reasonably, this 'offset' decorrelation is due to additional decorrelation sources such as muscle movements and dynamic scattering events with red blood cells (RBCs) along the photon path to the focal plane. We hypothesized that the total ACF can be regarded as the product of the two (statistically-independent) ACF's describing the offset and flow dynamics [10, 11], and the actual flow  $\tau_c$  can be derived from a simple equation (Eq. 3.9) that can be practically solved by selecting  $\tau_c$ 's from the vessel and adjacent tissue regions defined from conventional SDF-images. The offset-corrected  $1/\tau_c$  vs flow relationship (Fig. 3.7) exhibited a higher linear correlation ( $r^2 = 0.95$ ) as compared to the uncorrected relationship ( $r^2 = 0.4$ ), substantiating our hypothesis. The offset-correction provides a method to find the  $\tau_c$  belonging to the desired RBC dynamics only and can be regarded as a first step towards quantitative laser speckle flowmetry.

Chapter 3 also revealed that the slope of the graph of  $1/\tau_c$  vs.  $V$  *in vitro* was much steeper compared to  $1/\tau_c$  vs.  $V$  *in vivo*, possibly caused by the smaller scatterer size and increase in number of dynamic scattering events *in vitro*. These findings were a motivation to perform a flow phantom experiment with varying size and concentration of flowing scatterers to assess the influence on the slope, designated as the proportionality factor  $\alpha$  in the relationship  $1/\tau_c = \alpha V$ . The outcome of this experiment forms the basis of Chapter 4. The experiment confirmed that  $\alpha$  changes with both size and concentration of flowing scatterers which is thus important to take into account for quantitative flowmetry. To generalize these results we modelled the experiment following the theoretical frameworks of DWS and Laser Doppler Flowmetry (LDF), modified to LSCI and our measurement geometry and optical properties. In this model, the scattering phase function of the flowing scatterers and the number of scattering events in the flow tube or blood vessel influence  $\alpha$ . The scattering phase function can be predicted using our recent advances in the modelling of optical scattering of whole blood using Mie and Percus-Yevick theories [12-15], and the number of scattering events by Monte Carlo simulations [16, 17]. Under certain conditions, which are met in SDF-LSCI of the *in-vivo* microcirculation, the theory and experiment match perfectly. In Chapter 4 we have thus further quantified laser speckle flowmetry by modelling and validating the relationship between  $\tau_c$  and flow velocity for the *in vivo* microcirculation.

Together, chapters 3 and 4 provide practical guidelines towards quantitative *in vivo* flowmetry which can be summarized as: a multi-exposure acquisition scheme to reliably estimate  $\tau_c$ ; a correction for additive decorrelation sources by measuring the  $\tau_{c,offset}$  from tissue regions; model-based scaling of  $\tau_c$  for multiple scattering where the number of scattering events in the vessel ( $N$ ) can be estimated from the vessel diameter; and relating this final  $\tau_c$  to the actual flow velocity through the proportionality constant  $\alpha$ . With the flow velocities at hand further quantitative assessment of the vessel blood flow (blood volume/time) and tissue perfusion (blood volume/tissue volume/time) can be made, since vessel diameters and vessel density can be found from the images. Though intuitively it may seem that the conventionally measured uncorrected decorrelation time relates to tissue perfusion (since it is a measure of multiple dynamic scattering events in tissue and flow velocity), important to keep in mind is that flow velocity and multiple scattering are not linearly related ( $1/\tau_c \neq \alpha'VN$  but  $1/\tau_c = \alpha'VA(N)$ , where  $\alpha'$  denotes  $\alpha$  for single scattering and  $A(N)$  is a model-based scaling factor, Chapter 4) and  $N$  is not linearly related to vessel diameter. Furthermore, our approach differentiates between measurement dynamics (due to blood

flow, muscle movements, laser stability, etc.) and the clinically relevant vessel dynamics (due to blood flow). In addition, an estimate of  $V$  and vessel diameter distribution are clinically relevant parameters for microcirculation functionality as well. Therefore, our model represents an improvement compared to previous reports on tissue dynamics using LDF, LSCI or DWS where this differentiation is not made, and creates new opportunities for the assessment of the microcirculation in studies within and between organs and organisms or during the course of disease and therapy.

### 8.2.2 Feasibility of LSCI for clinical microcirculation imaging

The initial motivation to integrate SDF with LSCI as clinical microcirculation imager was the inability of SDF to measure microcirculatory perfusion automatically. The sequential steps for quantitative flowmetry using SDF-LSCI as summarized in the previous paragraph can straightforwardly be automated to enable instantaneous measurements at the bedside or during operations. In addition, SDF-LSCI is sensitive to higher flow velocities than conventional SDF imaging. Flow velocities as high as 20 mm/s were validated in this thesis (compared to  $<2$  mm/s for SDF). Higher flows will be clearly visible in speckle contrast images and if their quantification is desirable the multi-exposure speckle acquisition should be extended towards shorter exposure times. Lastly, SDF-LSCI utilizes wavelengths where the absorption by blood is low (red to NIR range) resulting in deeper light penetration and the potential to image through scattering layers such as the skin. In this case, the vessel diameters can only be estimated from SDF-LSCI images instead of conventional-SDF images. The latter is also important in view of conventional LSCI set-ups, where no absorption-based SDF images of blood vessel can be captured. Vessel and tissue regions can still be identified from the speckle contrast (or decorrelation time) images, although the contrast decreases in the case of low flows. Monte Carlo simulations verified that the number of scattering events in the vessels is similar in both geometries. The results on quantitative SDF-LSCI from chapters 3 and 4 are thus generally applicable to laser speckle flowmetry, and, by the analogy explained in chapter 2, also to LDF imaging systems.

The function of the microcirculation is to supply the tissue with oxygen and nutrients according to its metabolic needs. An impaired microcirculation is an important pathological marker for various diseases and is the cause and the consequence of clinical pathologies, as outlined in Chapter 1 [18]. The reinstated quantitiveness of the LSCI technique facilitates the comparison of blood flow, velocity and tissue perfusion between different spatial locations or time points, where previously semi-quantitative measures of flow [19, 20], or relative changes in blood flow velocity necessitating a baseline measurement [4, 21], were reported. Quantitative LSCI enables the monitoring of the chronic changes of cerebral perfusion after ischemic stroke [22, 23], vascular remodelling during the healing process in burn wounds [24, 25], or the comparison of microcirculatory perfusion in several organs during septic shock models [26]. The sensitivity to higher flows is instrumental for studying brain metabolism, since blood flow velocities in rat cerebral capillaries were reported up to 2.8 mm/s (venules and venous capillaries) and 21 mm/s (arterioles and arterial capillaries) measured using incident light microscopy and transit time photometry [27]. The control mechanisms of cerebral capillary flow are subject to controversy [28]. A current hypothesis suggesting that neurological signals regulate the capillary flow by triggering the precapillary arterioles, would benefit from quantitative LSCI as a simple non-invasive technique to

visualize capillary flow velocity *in vivo*. Cerebral capillary flow control is clinically relevant for e.g. research on functional brain activation, epilepsy, migraine, head trauma, ischemia and hypoxia [28]. The ability to quantify microcirculatory flows through skin has potential applications in neonatal care, where the correlation between baseline microvascular blood flow as measured with LDF on the lower limb, exhibits significant relationships with clinical illness severity and cardiovascular function in the immediate postnatal period [29, 30]. The application of quantitative LSCI may increase the clinical relevancy by providing information on microcirculation geometry and blood flow velocity non-invasively for this vulnerable group of patients in the neonatal intensive care unit.

## 8

### 8.2.3 Sensitivity to low flows

A current shortcoming of LSCI is the low sensitivity to low flows, for which the offset and flow decorrelation times are very similar and there is hardly any contrast between vessel and tissue. This is aggravated in ‘active’ tissue such as the tongue measured using a hand-held device. In our *in vivo* experiments flows as low as 0.3 mm/s were quantified by SDF-LSCI. In sepsis, sluggish (< 0.3 mm/s) and interrupted blood flows are indicated as important parameters [31, 32]. Fortunately, the integration of SDF with LSCI allows for an improvement in the analysis that can potentially enhance the sensitivity to lower blood flows: regions belonging to one vessel (same flow velocity) can be outlined according to the conventional-SDF images to serve as the local region to calculate  $K$ , if needed extended temporally as well. This image-based determination of local region results in a larger local region, thus a more reliable estimation of  $K$  while also providing a higher spatial and temporal resolution. Since all pixels in the local region represent the same flow, the accuracy and sensitivity to lower flows is likely improved.

### 8.2.4 Multiple populations of dynamic photons

The offset-correction as presented in this thesis assumes that the photons detected at the vessel region have been subject to offset decorrelation events and subsequently to at least one dynamic scattering event in the vessel, justifying Eq. 3.8:  $g_{1,total}(\tau) = g_{1,flow}(\tau) \cdot g_{1,offset}(\tau)$ . Consequently, multi-exposure speckle contrast curves representing the total decorrelation would always show faster decorrelation than the flow-only decorrelation curve. To test this, we designed a phantom set-up where a nylon thread with a roughened surface was pulled through a tube embedded in a dynamic medium (titanium dioxide in 30% glycerol), and in a static medium (titanium dioxide in silicone) as used in Chapters 3 and 4. Preliminary results are shown in Fig. 8.1 a. The multi-exposure  $K$ -curve for ‘flow’ in the static medium can be regarded as due to flow only (as the medium is static) and the multi-exposure  $K$ -curve for ‘flow’ in the dynamic medium can be regarded as the total decorrelation due to flow and offset decorrelation. The dynamic phantom shows that for the velocity of 10 mm/s ( $\tau_{c,flow} < \tau_{c,offset}$ ) the total decorrelation is *not* faster than the decorrelation due to flow only (square data points), and Eq. 3.8 breaks down. Generally, we saw that for the dynamic phantom the multi-exposure curves for flow and offset regions were mutually influenced by each other’s dynamics, which is caused by scattering of photons from the flow region into the offset region and vice versa. This means that at any position in the image the decorrelation is influenced by both ‘offset’ and ‘total’ (flow + offset) photons. Therefore, the autocorrelation functions describing both processes cannot be directly multiplied. A possible way to correct for this is to define a third population of photons contributing to

the (fluctuating) electric field:  $E(t) = E_{f,total}(t) + E_{f,offset}(t) + E_s(t)$ . Subsequently the Siegert relation can be modified accordingly and the speckle equation can be derived similar as before (Chapter 2.3). The K-curves resulting from two dynamic populations (total and offset) with different  $\tau_c$ 's for flow and offset are plotted in fig. 8.1b (dark and light green lines), together with the K-curves resulting from one (flow) population (dark and light red lines), the  $\tau_c$ 's are chosen to reflect the situation in Fig. 8.1a and the relative population of offset (and total) photons is set to 0.5. The calculated K-curves derived from multiple dynamic photon populations in Fig. 8.1b mimic the dynamic phantom experiment, supporting this approach. In practice, fitting the model presented in Fig. 8.1b is complicated because a large (and closely spaced) range of exposure times is required for a reliable fit. The dynamic phantom experiment exaggerates the biological situation by the highly scattering medium covering the tube ( $\mu'_s = 1.7 \text{ mm}^{-1}$ , as compared with the low scattering non-keratinized epithelium layer covering the sublingual microcirculation) giving rise to a large population of offset photons detected at the flow (vessel) region. A lower fraction of offset photons for sublingual vessel regions is expected due to the high scattering coefficient of blood and the transparent epithelium top layer. The excellent results of Chapters 3 and 4 based on Eq. 3.8 verify this. However, the presence of multiple populations of dynamic photons is worth exploring further especially when using LSCI through highly scattering layers such as skin.

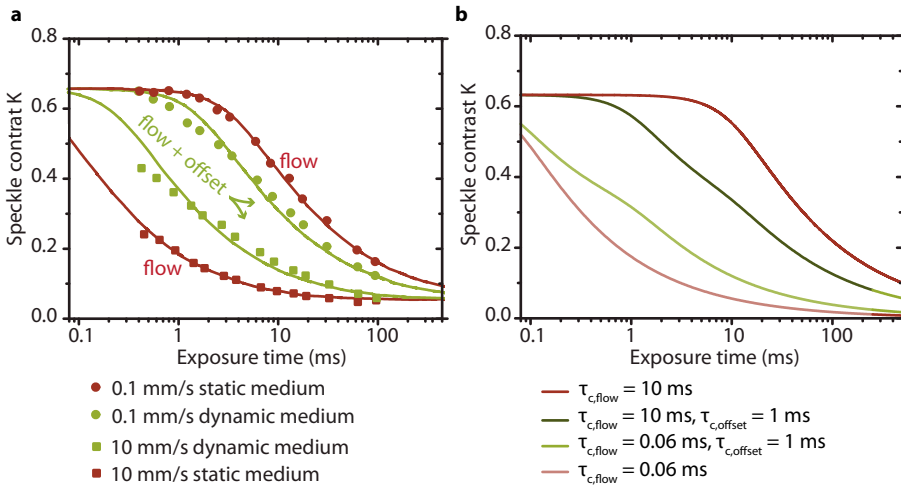


**Fig. 8.1 | Dynamic medium flow phantom experiment (unpublished results).** (a) Multi-exposure K-curves and corresponding fit of Eq. 3.7 or 4.10 for a moving thread in static (red curves/data points) and dynamic (green curves/data points) medium (b) Multi-exposure K-curves according to Eq. 3.7/4.10 ( $\beta = 0.4, \rho = 1$ ) for 2 different  $\tau_c$ 's (light red [ $\tau_{c,flow} = 0.06 \text{ ms}$ ] and dark red [ $\tau_{c,flow} = 10 \text{ ms}$ ]) and multi-exposure K-curves resulting from 2 populations of dynamic photons (50% offset, 50% total; light green [ $\tau_{c,flow} = 0.06 \text{ ms}, \tau_{c,offset} = 1 \text{ ms}$ ], dark green [ $\tau_c = 10 \text{ ms}, \tau_{c,offset} = 1 \text{ ms}$ ]).

### 8.2.5 Conclusions on laser speckle flowmetry

Answering the question: is laser speckle flowmetry a quantitative tool? remains a controversial topic. Using SDF-LSCI as outlined in this thesis can be regarded as considerably quantitative and opportunities for enhancing the accuracy and sensitivity as outlined in Section 8.2.3 are promising. Two bottlenecks in quantitative laser speckle flowmetry, the quantification of  $a$  and influence of multiple scattering, have been addressed in this thesis. Both findings can be applied to conventional LSCI set-ups and LDF techniques as well, thereby contributing to the quantitateness of many flowmetry applications. The technological simplicity of LSCI set-ups, combined with the potential for automated and quantitative analysis of flow velocities, sensitivity to a large flow range and the ability to measure through scattering layers summarize the advantages of LSCI as clinical microcirculation imager.

## 8.3 UCNPs FOR THE DELIVERY OF CONTRAST ENHANCING AGENTS TO TUMOURS

### 8.3.1 Key results on imaging Upconversion Nanoparticles in biological tissue

Chapters 5 through 7 show that upconversion nanoparticles (UCNPs) are a valuable addition to the collection of photoluminescent agents in biomedical imaging, where the usefulness greatly depends on the provided signal to background ratio (or contrast). The key optical properties of UCNPs enable autofluorescence-free imaging due to a nonlinear upconversion process at relatively low excitation intensities with long (sub-millisecond) lifetimes [33]. The remaining background signal consisting of detector noise and excitation light leaking through the filters can be minimized by time-gated detection and scientific grade cooled detectors, advancing towards signal shot noise limited imaging. In view of these optical and detection features, the UCNP imaging contrast is highly dependent on the conversion efficiency. Therefore, we started with designing an integrating sphere set-up to quantify the conversion efficiency versus the excitation intensity, as detailed in Chapter 6. The subsequent assessment of the imaging and detection throughput of the wide-field inverted epi-fluorescent microscope (used in Chapters 6 and 7) operating in continuous wave mode, enabled the quantitative modelling of UCNP-based microscopic imaging. With this system, single particle imaging and hyperspectral imaging confirmed that the ensemble and single UCNP had identical optical properties, which is important to link ensemble measurements [34-37] to discrete particle studies [38, 39]. The experimental detection of a single UCNP through 250  $\mu\text{m}$  haemolysed blood and theoretical estimation of single particle detection in skin-depths up to 400  $\mu\text{m}$  under optimized conditions (pulsed excitation allowing higher excitation intensity and time-gated detection) illustrate the high-sensitivity imaging that is achievable using UCNPs. Due to the rapid reduction of contrast with imaging depth in tissue, caused by the scattering-induced excitation attenuation and nonlinear UCNP emission, the high potential applications include UCNP-guided imaging at relatively superficial depths ( $< 1$  cm) such as *in vitro* thick slices, biological liquids or bioassays, or *in vivo* subsurface structures [40-42]. For these scenarios the detection of small amounts of UCNPs is feasible and opens up possibilities for the detection of a small amount of biomarkers [43, 44] or cells [45, 46], including *in vivo* cell tracking [47]. A promising application is the intraoperative use of UCNPs to guide the surgeon to areas suspect to contain tumour cells. To enhance the tumour-to-tissue contrast, specific labelling of tumour cells is helpful which was addressed in Chapter 7. The UCNPs were biofunction-

alized with mini-antibodies that specifically targeted the human epidermal growth factor receptor (Her2/neu) overexpressed by SK-BR-3 breast cancer cells, resulting in specific labelling of tumour cells in a 10:1 ratio to control cells *in vitro*. The labelled breast cancer cells were covered with breast tissue simulating optical phantom layers that mimicked the optical scattering and absorption properties of breast tissue. The UCNP signal coming from the monolayer of breast cancer cells was detected through a maximum of 1.6 mm phantom thickness, which was a substantial imaging depth considering the low amount of the labelled cells (< 10 cells) in the image. Using the calibrated imaging and detection properties of the imaging system (such as spectral throughput, detector sensitivity) and UCNP optical signal quantification, the number of UCNP per cell could be estimated and projected onto an *in vivo* scenario of imaging a small breast cancer lesion embedded in breast tissue. As detailed in Chapter 7, the estimated detection depth of the small lesion was up to 4 mm, which is superior compared to the detection depth estimated using Cy5 (an organic fluorescent NIR dye) as tumour labelling agent being  $\sim 2.5$  mm [48]. The latter result was estimated from human melanoma bearing mice, and the study additionally revealed an improved long-term survival rate for mice subject to fluorescence guided tumour resection as compared with the control group operated under white light conditions. The improved contrast using upconversion-based photoluminescence would potentially improve the survival rate even further, since a detection depth of several millimetres is clinically relevant e.g. during tumour resections.

Besides the identification and experimental assessment of application niches of UCNP, chapters 6 and 7 also presented the experimental validation of optical signal modelling in absorbing and scattering media based on Lambert-Beers law. The theoretical model presented in Chapter 6 showed excellent agreement with the experimental results of the phantom study in Chapter 7 (Fig. 7.7, *in vitro* signal data and model), changing only the different model parameters such as objective numerical aperture (NA), optical properties of the tissue (skin in Chapter 6 vs. breast tissue in Chapter 7), number of UCNP (single in Chapter 6 vs. cluster of labelled cells in Chapter 7) and their optical properties (absorption cross-section and conversion efficiency). The Lambert-Beer model modified using the transport attenuation coefficient (instead of the usual absorption coefficient) was applied to calculate the reduction of excitation intensity with depth in tissue and the reduction of the signal intensity on the return path to the detector. This model implies that photons that have been absorbed or isotropically scattered are removed from the signal calculation, unlike previously reported models based on photon diffusion approximations [49]. Though the higher tissue scattering coefficient as compared with the absorption coefficient at the UCNP excitation and emission wavelengths validate the use of the diffusion approximation, the application of a diffusion-based model did not agree with our results. A possible explanation is the high-NA objective used for imaging, effectively rejecting out of focus (diffuse) photons in the set-up. By changing the model parameters as required, our UCNP tissue imaging model is instrumental for the quantitative assessment of potential UCNP-based imaging scenarios.

### 8.3.2. *In vivo* application of UCNP

The evaluation of UCNP properties in the context of *in vivo* situations is crucial for the translation of UCNP from the lab to clinical applications. An identified purpose in this

thesis is the delivery of UCNP through the leaky tumour vasculature for enhanced detection and/or tumour therapy. In view of this, a versatile model is the chick embryo chorioallantoic membrane (CAM), an extra-embryonic vascularised membrane responsible for the gas exchange of the developing chick embryo. The development of protocols describing *ex ovo* culturing of chick embryos by transferring the embryo into a sterile container, enabled exposure of the CAM and easy access for intervention and imaging [50, 51]. Since the embryos are immune-deficient (up to embryonic development day 14) foreign cancer cells can be introduced without rejection. Grafting tumour cells on the CAM results in their adoption by the CAM and subsequent tumour-induced angiogenesis enables their growth into proliferating, vascularised tumours [52, 53]. The CAM-based tumour development and their microvascular environment can be studied in detail [54, 55]. The presence of nearly all relevant stroma factors e.g. immune cells (at a later stage), extracellular matrix components, blood and lymphatic vessels make the CAM model highly suited for studying tumour-stroma interactions, tumour metastasis, and therapy-induced changes in tumour development, implying the upcoming role of the CAM model in cancer research [56].

The characteristics of the CAM tumour model are useful to study the delivery of nanoparticles to tumours, as was shown by the delivery of macromolecules like fluorescent dextran [57] and virus-derived fluorescently labelled nanoparticles [58] to the CAM tumour sites through the leaky tumour vasculature. Following the *in vitro* results of Chapters 6 and 7, utilizing the CAM tumour model is an appropriate next step in the assessment of UCNP for contrast-enhanced tumour detection. As elucidated in Chapter 5, UCNP should not only exhibit advantageous optical properties but also excellent biochemical properties for effective *in vivo* application, including surface properties that offer a good dispersability in buffers and ensure biocompatible interaction with tissues. Biocompatible surface properties prevent or delay the uptake by the immune system thereby increasing the nanoparticle circulation times. In addition, the biocompatible surface provides functional groups for the binding of molecules (antibodies/ligands) with tumour-specific targeting properties. Long circulation times enhance the probability that the particles will end up in the tumour and facilitate enhanced tumour visibility or induce therapy. Feedback on the UCNP chick embryo circulation time is thus meaningful for UCNP design. Preliminary results on the quantification of UCNP circulation times in chick embryos are presented in Fig. 8.2. The UCNP were synthesized in-house, coated with a silica shell and subsequently functionalized to produce three different groups: carboxyl (COOH, negatively charged), amine (NH<sub>2</sub>, positively charged) and polyethylene-glycol (PEG, neutral) functionalized UCNP. At several time points after injection of the UCNP (50 µL of 0.5 mg/ml UCNP solution) a small amount of blood (5 µL) was drawn from the embryos and blood smears were prepared on glass slides as shown in Fig. 8.2c. For each slide the UCNP signal was quantified using the inverted microscope set-up described in Chapter 6. The results (based on 3 different chicks per functional groups) show a decreasing amount of UCNP in the blood with increasing time, where the PEGylated particles circulate the longest and can still be found after 12 hours of circulating. The quantification of circulation time can tailor the future design of UCNP with other functional surface groups (e.g. amphiphilic polymers) to optimize biochemistry protocols while maintaining long circulation times.

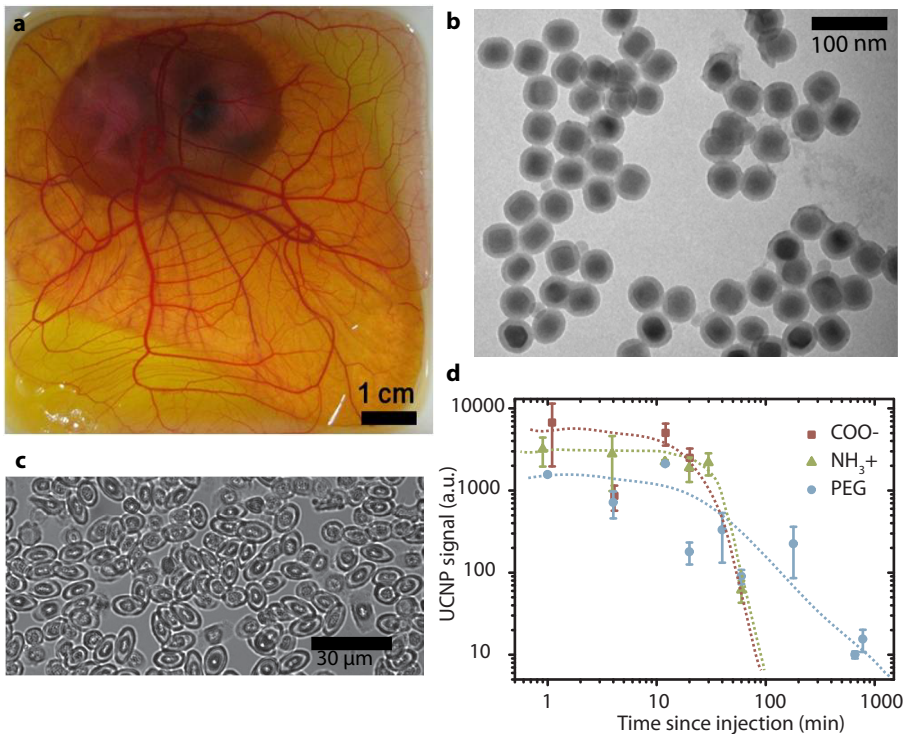


**Fig. 8.2 | Chick embryo model for the assessment of UCNP circulation times** (unpublished results). (a) Ex ovo chick embryo at embryonic development day 8. (b) TEM images of UCNPs coated with silica shell before subsequent functionalization. (c) Bright field image of chick embryo blood smear on glass slide. (d) UCNP signal from blood smears sampled at different time points after injection, quantified using epiluminescence microscopy.

The next step is the development of vascularised tumours in the chick embryo model. Tumours can be grafted on the CAM by mildly scratching the membrane before placing tumour spheroids [59, 60], tumour cell soaked gelatine-sponges [61], tumour cells resuspended in Matrigel [62], or simply a drop of tumour cells on the affected region of the membrane [57]. We evaluated different tumour cell lines and tumour grafting methods, demonstrating successful tumour growth and vascularisation as shown in Fig. 8.3. In Fig. 8.4 our first published results are shown presenting targeted labelling of small tumours (MCF7 breast cancer cells) by UCNPs functionalized with tumour-specific antibodies [63].

The CAM tumour model represents an interesting method for further development of UCNP-based detection of small tumour lesions, with the proof-of-principle shown in Fig. 8.4. The long exposure time of 2 minutes in spite of the superficial location of the tumour indicates that improved detection of UCNP-labelled tumours is a necessity for practical application of UCNPs, for example for intraoperative diagnosis. On the one hand the UCNP signal could be enhanced by doping the UCNPs with Thulium ions instead of Erbium ions which have a large emission peak at 800 nm (see Figure 5.3), for which tissue attenuation is reduced. In addition, a 70-fold increase of conversion efficiency was shown for UCNPs with a high Tm-dopant concentration (8%) at high excitation intensity [64]. Further improvements include the increase of the absorption cross-section by utilizing ‘antenna effects’ from dyes,

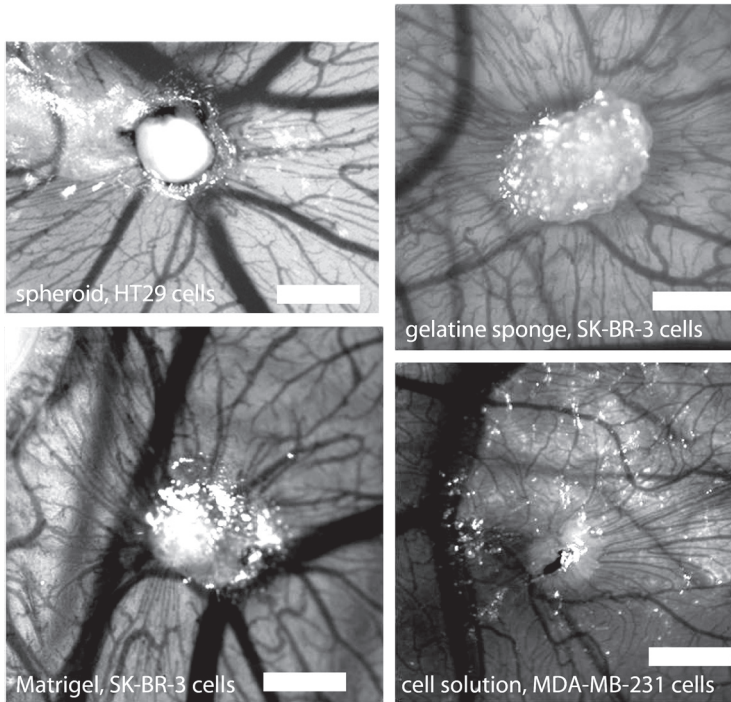


**Fig. 8.3 | Chick embryo chorioallantoic membrane (CAM) with tumours.** Growth and vascularisation of tumours, 7 days after grafting of tumour cells on chick embryo CAM using spheroids, gelatine sponges, Matrigel or cell solutions containing HT29 (Human colorectal adenocarcinoma), SK-BR-3 or MDA-MB-231 (human breast cancers) cells. Scale bar represents 250 µm.

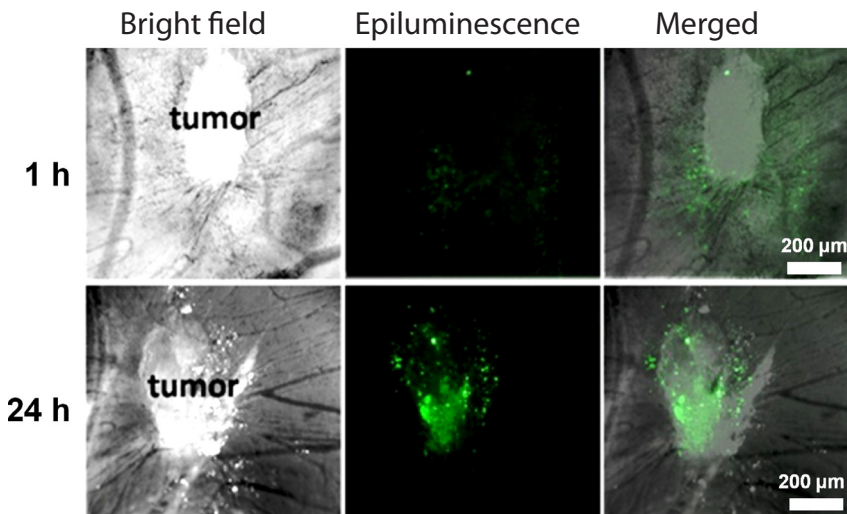


**Fig. 8.4 | Targeted labelling of tumour spheroids grafted on the chick embryo CAM.** Antibody-labelled UCNPs were imaged at the tumour region at 1 h (top row) and 24h (bottom row) after injection. From left to right are bright field, epiluminescence (980 nm) and merged intravital microscope images at 4x magnification and 2 minutes exposure time. Adapted from ref. [63]

plasmons, quantum dots or other doping elements with a strong absorption to sensitize the UCNPs [42], or shifting the excitation wavelength to 800 nm by adding  $\text{Nd}^{3+}$  as a second sensitizer [65]. On the other hand the excitation and detection efficiency can be improved by using high power pulsed laser excitation and time-gated detection mechanisms.

### 8.3.3 Cytotoxicity and non-specific cellular uptake of UCNPs

The previous results demonstrate the potential for UCNP-guided detection of small tumour lesions during operations. A remaining challenge is to ensure the biosafety of UCNPs through preclinical testing of the *in vivo* UCNP biochemical stability, cytotoxicity and systemic toxicity. We assessed the cytotoxicity effects of differently coated UCNPs as well as bare UCNPs on normal human skin cells in a recently published paper [66]. After 24h of incubation of the cells with UCNPs the lowest cytotoxicity was observed for bare and poly-lactide coated UCNPs (see Fig. 8.5a). Using the inverted microscope set-up described in Chapter 6 the non-specific cellular uptake of the UCNPs could also be quantified as presented in Fig. 8.5b. This study shows that cytotoxicity and cellular internalization strongly depend on coating, though the UCNPs do not exhibit intrinsic toxicity. This indicates that ongoing research is needed to design functional UCNP-coatings with increased biocompatibility and reduced cytotoxicity.

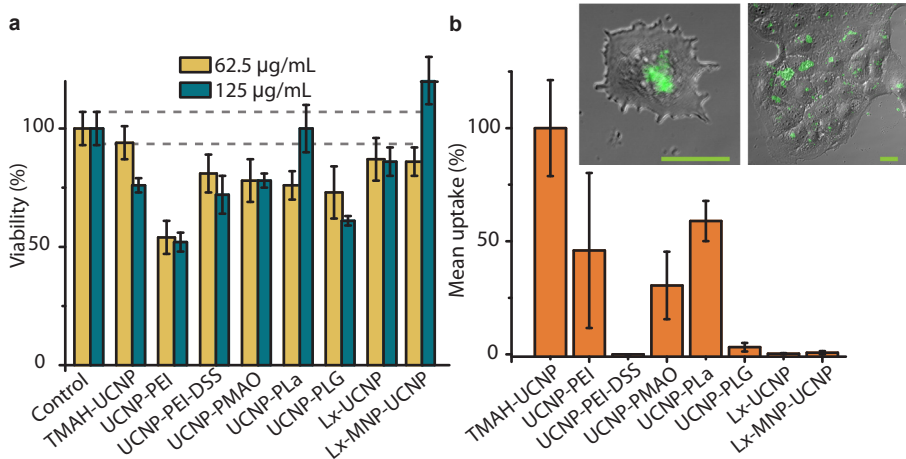


**Fig. 8.5 | Viability and cellular uptake of UCNPs in vitro.** (a) Bar plot of the viability of human skin cells (keratinocytes) 24h co-cultured with differently coated UCNPs (concentrations 62 µg/mL yellow and 125 µg/mL green bars). Error bars are 95% confidence interval (CI) of the mean. Control sample viability was set to 100%; grey dashed lines represent the control group's 95% CI. TMAH-UCNP represent bare uncoated particles, and PEI, PEI-DSS, PMAO, PLA and PLG are amphiphilic polymer coatings detailed in Chapter 5. (b) Non-specific cellular uptake of bare and differently coated UCNPs by human skin cells (keratinocytes) after 24h co-culturing (concentration: 125 µg/mL), normalized for the bare UCNP uptake (100%). Inset: merged bright field and luminescence image of a single cell and a monolayer of cells exposed to bare TMAH-UCNPs. Scale bar, 20 µm. Adapted from ref [66].

#### **8.3.4 Conclusion on upconversion nanoparticles**

The group of photoluminescent nanoparticles assessed in this thesis, nominated as upconversion nanoparticles, has considerable advantages for imaging applications in the biomedical context. Particularly the background-free imaging possibility allows imaging of small amounts of particles, expanding the possibilities for imaging of small lesions or minute amounts of biomarkers. Realization of high-sensitivity UCNP-aided imaging warrants further research in two key areas: improving the UCNP brightness and detection sensitivity; and improving the biocompatibility to enhance molecular contrast and provide meaningful results for clinical applications.

## 8.4 REFERENCES

1. J. W. Goodman, *Speckle phenomena in optics: theory and applications* (Roberts and Company Publishers, Greenwood Village, CO, 2007).
2. A. Fercher and J. Briers, "Flow visualization by means of single-exposure speckle photography," *Opt. Commun.* **37**, 326-330 (1981).
3. D. D. Duncan and S. J. Kirkpatrick, "Can laser speckle flowmetry be made a quantitative tool?," *JOSA A* **25**, 2088-2094 (2008).
4. A. B. Parthasarathy, S. Kazmi, and A. K. Dunn, "Quantitative imaging of ischemic stroke through thinned skull in mice with Multi Exposure Speckle Imaging," *Biomedical optics express* **1**, 246-259 (2010).
5. J. C. Ramirez-San-Juan, R. Ramos-García, I. Guizar-Iturbide, G. Martínez-Niconoff, and B. Choi, "Impact of velocity distribution assumption on simplified laser speckle imaging equation," *Opt. Express* **16**, 3197-3203 (2008).
6. D. A. Boas and A. K. Dunn, "Laser speckle contrast imaging in biomedical optics," *J. Biomed. Opt.* **15**, 011109-011109-011112 (2010).
7. A. B. Parthasarathy, W. J. Tom, A. Gopal, X. Zhang, and A. K. Dunn, "Robust flow measurement with multi-exposure speckle imaging," *Opt. Express* **16**, 1975-1989 (2008).
8. L. M. Richards, S. Kazmi, J. L. Davis, K. E. Olin, and A. K. Dunn, "Low-cost laser speckle contrast imaging of blood flow using a webcam," *Biomedical optics express* **4**, 2269-2283 (2013).
9. K. R. Forrester, J. Tulip, C. Leonard, C. Stewart, and R. C. Bray, "A laser speckle imaging technique for measuring tissue perfusion," *Biomedical Engineering, IEEE Transactions on* **51**, 2074-2084 (2004).
10. D. Bicout and G. Maret, "Multiple light scattering in Taylor-Couette flow," *Physica A: Statistical Mechanics and its Applications* **210**, 87-112 (1994).
11. D. Durian, "Accuracy of diffusing-wave spectroscopy theories," *Physical Review E* **51**, 3350 (1995).
12. N. Bosschaert, G. J. Edelman, M. C. Aalders, T. G. van Leeuwen, and D. J. Faber, "A literature review and novel theoretical approach on the optical properties of whole blood," *Lasers in medical science* **29**, 453-479 (2014).
13. J. K. Percus and G. J. Yevick, "Analysis of classical statistical mechanics by means of collective coordinates," *Physical Review* **110**, 1 (1958).
14. M. Wertheim, "Exact solution of the Percus-Yevick integral equation for hard spheres," *Physical Review Letters* **10**, 321-323 (1963).
15. H. C. Hulst, *Light scattering by small particles* (Courier Dover Publications, 1957).
16. F. F. M. de Mul, "Monte-Carlo simulation of light transport in Turbid Media," in *Handbook of Coherent Domain Optical Methods, Biomedical Diagnostics, Environment and Material Science*, V. V. Tuchin, ed. (Kluwer Publishers, 2004), pp. 465-533.
17. F. F. M. de Mul, M. H. Koelink, M. L. Kok, P. J. Harmsma, J. Greve, R. Graaff, and J. G. Aarnoudse, "Laser Doppler velocimetry and Monte Carlo simulations on models for blood perfusion in tissue," *Applied optics* **34**, 6595-6611 (1995).
18. B. Fagrell and M. Intaglietta, "Microcirculation: its significance in clinical and molecular medicine," *J. Intern. Med.* **241**, 349-362 (1997).
19. A. Rege, K. Murari, A. Seifert, A. P. Pathak, and N. V. Thakor, "Multiexposure laser speckle contrast imaging of the angiogenic microenvironment," *Journal of biomedical optics* **16**, 056006-056006-056010 (2011).
20. R. Bezemer, E. Klijn, M. Khalilzada, A. Lima, M. Heger, J. van Bommel, and C. Ince, "Validation of near-infrared laser speckle imaging for assessing microvascular (re) perfusion," *Microvascular Research* **79**, 139-143 (2010).
21. A. B. Parthasarathy, E. L. Weber, L. M. Richards, D. J. Fox, and A. K. Dunn, "Laser speckle contrast imaging of cerebral blood flow in humans during neurosurgery: a pilot clinical study," *J. Biomed. Opt.* **15**, 066030-066030-066038 (2010).
22. S. M. S. Kazmi, A. B. Parthasarathy, N. E. Song, T. A. Jones, and A. K. Dunn, "Chronic imaging of cortical blood flow using Multi-Exposure Speckle Imaging," *Journal of Cerebral Blood Flow & Metabolism* **33**, 798-808 (2013).
23. A. K. Dunn, H. Bolay, M. A. Moskowitz, and D. A. Boas, "Dynamic imaging of cerebral blood flow using laser speckle," *J. Cereb. Blood Flow Metab.* **21**, 195-201 (2001).
24. W. K. Stadelmann, A. G. Digenis, and G. R. Tobin, "Physiology and healing dynamics of chronic cutaneous wounds," *The American Journal of Surgery* **176**, 265-385 (1998).
25. C. Stewart, R. Frank, K. Forrester, J. Tulip, R. Lindsay, and R. Bray, "A comparison of two laser-based methods for determination of burn scar perfusion: laser Doppler versus laser speckle imaging," *Burns* **31**, 744-752 (2005).

26. L. B. Hildebrand, V. Krejci, A. Banic, D. Erni, A. M. Wheatley, and G. H. Sigurdsson, "Dynamic study of the distribution of microcirculatory blood flow in multiple splanchnic organs in septic shock," *Crit. Care Med.* **28**, 3233-3241 (2000).
27. Y. Ma, A. Koo, H. Kwan, and K. Cheng, "On-line measurement of the dynamic velocity of erythrocytes in the cerebral microvessels in the rat," *Microvasc. Res.* **8**, 1-13 (1974).
28. Y. Itoh and N. Suzuki, "Control of brain capillary blood flow," *J. Cereb. Blood Flow Metab.* **32**, 1167-1176 (2012).
29. M. J. Stark, V. L. Clifton, and I. M. Wright, "Microvascular flow, clinical illness severity and cardiovascular function in the preterm infant," *Archives of Disease in Childhood-Fetal and Neonatal Edition* **93**, F271-F274 (2008).
30. M. J. Stark, V. L. Clifton, and I. M. Wright, "Sex-specific differences in peripheral microvascular blood flow in preterm infants," *Pediatr. Res.* **63**, 415-419 (2008).
31. D. De Backer, S. Hollenberg, C. Boerma, P. Goedhart, G. Büchele, G. Ospina-Tascon, I. Dobbe, and C. Ince, "How to evaluate the microcirculation: report of a round table conference," *Crit. Care* **11**, R101 (2007).
32. C. Ince, "The microcirculation is the motor of sepsis," *Critical Care* **9**, S13 (2005).
33. Z. Song, Y. G. Anissimov, J. Zhao, A. V. Nechaev, A. Nadort, D. Jin, T. W. Prow, M. S. Roberts, and A. V. Zvyagin, "Background free imaging of upconversion nanoparticle distribution in human skin," *Journal of biomedical optics* **18**, 061215-061215 (2013).
34. J.-C. Boyer and F. C. Van Veggel, "Absolute quantum yield measurements of colloidal NaYF<sub>4</sub>: Er<sup>3+</sup>, Yb<sup>3+</sup> upconverting nanoparticles," *Nanoscale* **2**, 1417-1419 (2010).
35. R. H. Page, K. I. Schaffers, P. A. Waide, J. B. Tassano, S. A. Payne, W. F. Krupke, and W. K. Bischel, "Upconversion-pumped luminescence efficiency of rare-earth-doped hosts sensitized with trivalent ytterbium," *JOSA B* **15**, 996-1008 (1998).
36. M. Pokhrel and D. K. Sardar, "High upconversion quantum yield at low pump threshold in Er<sup>3+</sup>/Yb<sup>3+</sup> doped La<sub>2</sub>O<sub>3</sub> phosphor," *Mater. Lett.* **99**, 86-89 (2013).
37. F. Wang, R. Deng, J. Wang, Q. Wang, Y. Han, H. Zhu, X. Chen, and X. Liu, "Tuning upconversion through energy migration in core-shell nanoparticles," *Nat. Mater.* **10**, 968-973 (2011).
38. S. Wu, G. Han, D. J. Milliron, S. Aloni, V. Altoe, D. V. Talapin, B. E. Cohen, and P. J. Schuck, "Non-blinking and photostable upconverted luminescence from single lanthanide-doped nanocrystals," *Proceedings of the National Academy of Sciences* **106**, 10917-10921 (2009).
39. S. Schietinger, L. d. S. Menezes, B. r. Lauritzen, and O. Benson, "Observation of size dependence in multicolor upconversion in single Yb<sup>3+</sup>, Er<sup>3+</sup> codoped NaYF<sub>4</sub> nanocrystals," *Nano Lett.* **9**, 2477-2481 (2009).
40. Y. Lu, J. Zhao, R. Zhang, Y. Liu, D. Liu, E. M. Goldys, X. Yang, P. Xi, A. Sunna, and J. Lu, "Tunable lifetime multiplexing using luminescent nanocrystals," *Nat. Photonics* (2013).
41. L. Xiong, Z. Chen, Q. Tian, T. Cao, C. Xu, and F. Li, "High contrast upconversion luminescence targeted imaging *in vivo* using peptide-labeled nanophosphors," *Anal. Chem.* **81**, 8687-8694 (2009).
42. G. Chen, H. Qiu, P. N. Prasad, and X. Chen, "Upconversion Nanoparticles: Design, Nanotechnology, and Applications in Theranostics," *Chem. Rev.* (2014).
43. Z. Chen, H. Chen, H. Hu, M. Yu, F. Li, Q. Zhang, Z. Zhou, T. Yi, and C. Huang, "Versatile synthesis strategy for carboxylic acid-functionalized upconverting nanophosphors as biological labels," *J. Am. Chem. Soc.* **130**, 3023-3029 (2008).
44. Y. Wang, P. Shen, C. Li, Y. Wang, and Z. Liu, "Upconversion fluorescence resonance energy transfer based biosensor for ultrasensitive detection of matrix metalloproteinase-2 in blood," *Anal. Chem.* **84**, 1466-1473 (2012).
45. Q. Liu, Y. Sun, T. Yang, W. Feng, C. Li, and F. Li, "Sub-10 nm Hexagonal Lanthanide-Doped NaLuF<sub>4</sub> Upconversion Nanocrystals for Sensitive Bioimaging *in vivo*," *J. Am. Chem. Soc.* **133**, 17122-17125 (2011).
46. M. Wang, C. Mi, Y. Zhang, J. Liu, F. Li, C. Mao, and S. Xu, "NIR-responsive silica-coated NaYbF<sub>4</sub>: Er/Tm/Ho upconversion fluorescent nanoparticles with tunable emission colors and their applications in immunolabeling and fluorescent imaging of cancer cells," *The Journal of Physical Chemistry C* **113**, 19021-19027 (2009).
47. N. M. Idris, Z. Li, L. Ye, E. K. Wei Sim, R. Mahendran, P. C.-L. Ho, and Y. Zhang, "Tracking transplanted cells in live animal using upconversion fluorescent nanoparticles," *Biomaterials* **30**, 5104-5113 (2009).
48. Q. T. Nguyen, E. S. Olson, T. A. Aguilera, T. Ji-

- ang, M. Scadeng, L. G. Ellies, and R. Y. Tsien, "Surgery with molecular fluorescence imaging using activatable cell-penetrating peptides decreases residual cancer and improves survival," *Proceedings of the National Academy of Sciences* **107**, 4317-4322 (2010).
49. C. Vinegoni, D. Razansky, S. A. Hilderbrand, F. Shao, V. Ntziachristos, and R. Weissleder, "Transillumination fluorescence imaging in mice using biocompatible upconverting nanoparticles," *Opt. Lett.* **34**, 2566-2568 (2009).
  50. D. S. Dohle, S. D. Pasa, S. Gustmann, M. Laub, J. H. Wissler, H. P. Jennissen, and N. Dünker, "Chick ex ovo culture and ex ovo CAM assay: how it really works," *Journal of visualized experiments: JoVE* (2009).
  51. H. C. Yalcin, A. Shekhar, A. A. Rane, and J. T. Butcher, "An ex-ovo chicken embryo culture system suitable for imaging and microsurgery applications," *Journal of visualized experiments: JoVE* (2010).
  52. H. Sun, J. Jia, X. Wang, B. Ma, L. Di, G. Song, and J. Ren, "CD44+/CD24- breast cancer cells isolated from MCF-7 cultures exhibit enhanced angiogenic properties," *Clin. Transl. Oncol.* **15**, 46-54 (2013).
  53. D. Ribatti, B. Nico, A. Vacca, L. Roncali, P. H. Burri, and V. Djonov, "Chorioallantoic membrane capillary bed: A useful target for studying angiogenesis and anti-angiogenesis *in vivo*," *The Anatomical Record* **264**, 317-324 (2001).
  54. E. I. Deryugina and J. P. Quigley, "Chick embryo chorioallantoic membrane model systems to study and visualize human tumor cell metastasis," *Histochem. Cell Biol.* **130**, 1119-1130 (2008).
  55. A. Zijlstra, J. Lewis, B. DeGryse, H. Stuhlmann, and J. P. Quigley, "The inhibition of tumor cell intravasation and subsequent metastasis via regulation of *in vivo* tumor cell motility by the tetraspanin CD151," *Cancer Cell* **13**, 221-234 (2008).
  56. M. Klingenberg, J. Becker, S. Eberth, D. Kube, and J. Wilting, "The chick chorioallantoic membrane as an *in vivo* xenograft model for Burkitt lymphoma," *BMC Cancer* **14**, 339 (2014).
  57. D. B. Pink, W. Schulte, M. H. Parseghian, A. Zijlstra, and J. D. Lewis, "Real-time visualization and quantitation of vascular permeability *in vivo*: implications for drug delivery," *PloS one* **7**, e33760 (2012).
  58. C. Choi-Fong, A. Amber, L. Hon-Sing, Z. Andries, and L. John, "Evaluation of nanoparticle uptake in tumors in real time using intravital imaging," *Journal of Visualized Experiments* (2011).
  59. J. Friedrich, C. Seidel, R. Ebner, and L. A. Kunz-Schughart, "Spheroid-based drug screen: considerations and practical approach," *Nature protocols* **4**, 309-324 (2009).
  60. N. De Magalhaes, L.-H. L. Liaw, and M. Berns, "An instruction on the *in vivo* shell-less chorioallantoic membrane 3-dimensional tumor spheroid model," *Cytotechnology* **62**, 279-283 (2010).
  61. D. Ribatti, B. Nico, A. Vacca, and M. Presta, "The gelatin sponge-chorioallantoic membrane assay," *Nature protocols* **1**, 85-91 (2006).
  62. N. A. Lokman, A. S. Elder, C. Ricciardelli, and M. K. Oehler, "Chick chorioallantoic membrane (CAM) assay as an *in vivo* model to study the effect of newly identified molecules on ovarian cancer invasion and metastasis," *International journal of molecular sciences* **13**, 9959-9970 (2012).
  63. K. Liu, J. A. Holz, Y. Ding, X. Liu, Y. Zhang, T. Langping, X. Kong, B. Priem, A. Nadort, S. A. G. Lambrechts, M. C. G. Aalders, W. J. Buma, P. D. Y. Liu, and H. Zhang, "Targeted labeling of early-stage tumor spheroid in chorioallantoic membrane model with upconversion nanoparticles," *Nanoscale* (2014).
  64. J. Zhao, D. Jin, E. P. Scharfner, Y. Lu, Y. Liu, A. V. Zvyagin, L. Zhang, J. M. Dawes, P. Xi, and J. A. Piper, "Single-nanocrystal sensitivity achieved by enhanced upconversion luminescence," *Nat. Nanotechnol.* **8**, 729-734 (2013).
  65. J. Shen, G. Chen, A. M. Vu, W. Fan, O. S. Bilsel, C. C. Chang, and G. Han, "Engineering the Upconversion Nanoparticle Excitation Wavelength: Cascade Sensitization of Tri-doped Upconversion Colloidal Nanoparticles at 800 nm," *Advanced Optical Materials* **1**, 644-650 (2013).
  66. A. E. Guller, A. N. Generalova, E. V. Petersen, A. V. Nechaev, I. A. Trusova, N. N. Landyshev, A. Nadort, E. A. Grebenik, S. M. Deyev, A. B. Shekhter, and A. V. Zvyagin, "Cytotoxicity and non-specific cellular uptake of bare and surface-modified upconversion nanoparticles in human skin cells," *Nano Research* (2014).